Noncontact Measurement of the Local Mechanical Properties of Living Cells Using Pressure Applied via a Pipette

Daniel Sánchez,* Nick Johnson,† Chao Li,† Pavel Novak,* Johannes Rheinlaender,‡ Yanjun Zhang,* Uma Anand,§ Praveen Anand,§ Julia Gorelik,¶ Gregory I. Frolenkov,‖ Christopher Benham,** Max Lab,* Victor P. Ostanin,† Tilman E. Schäffer,‡ David Klenerman,† and Yuri E. Korchev*

*Division of Medicine, Imperial College London, Hammersmith Hospital Campus, London, W12 0NN, United Kingdom; †Department of Chemistry, University of Cambridge, Cambridge, CB2 1EW, United Kingdom; ‡Institute of Applied Physics, University of Erlangen-Nuremberg, 91058 Erlangen, Germany; §Peripheral Neuropathy Unit, Imperial College London, Hammersmith Hospital Campus, London, W12 ONN, United Kingdom; ¶National Heart and Lung Institute, Imperial College London, London SW3 6LY, United Kingdom; ‖University of Kentucky, Department of Physiology, Chandler Medical Center, Lexington, Kentucky 40536-0298; and **Neurology Centre of Excellence for Drug Discovery, Glaxo SmithKline Research and Development, New Frontiers Science Park (North), Harlow, Essex, CM19 5AW, United Kingdom

ABSTRACT Mechanosensitivity in living biological tissue is a study area of increasing importance, but investigative tools are often inadequate. We have developed a noncontact nanoscale method to apply quantified positive and negative force at defined positions to the soft responsive surface of living cells. The method uses applied hydrostatic pressure (0.1–150 kPa) through a pipette, while the pipette-sample separation is kept constant above the cell surface using ion conductance based distance feedback. This prevents any surface contact, or contamination of the pipette, allowing repeated measurements. We show that we can probe the local mechanical properties of living cells using increasing pressure, and hence measure the nanomechanical properties of the cell membrane and the underlying cytoskeleton in a variety of cells (erythrocytes, epithelium, cardiomyocytes and neurons). Because the cell surface can first be imaged without pressure, it is possible to relate the mechanical properties to the local cell topography. This method is well suited to probe the nanomechanical properties and mechanosensitivity of living cells.

INTRODUCTION

Mechanosensitivity is universally found in biological system (1), involving mechanosensitive ion channels (2–4), and many membrane and intracellular molecules and structures, including the cytoskeleton (5–7) and downstream intracellular signals (8). In many cases the whole cell may be regarded as a mechanosensor, and cellular mechanosensitivity is a study area of rapidly increasing importance (9). This demands continued development of investigative tools capable of probing the mechanical properties of membranes without damaging them, which is a challenge. Cells have a soft membrane supported by an internal cytoskeleton, thus the cell membrane is easily damaged if too large a force is applied. Also, as cell structure is not homogeneous, the local membrane mechanical properties will vary with the local site of the probe and the variation in mechanical properties is very likely to be related to cellular function.

The mechanical properties of cells have been measured using four main methods: micropipette aspiration (10), optical tweezers (11,12), microrheological methods based on single particle tracking (13), and atomic force microscopy (AFM) (14–23). However, AFM is the only method that has been used to map the local mechanical properties of a range of different cells on a nanoscale (14–23) and relate this to the cell topography. The mapping requires direct contact between the probe and the cell surface, and the membrane can adhere to the probe, which may contaminate the probe making repetitive experiments impossible. Furthermore, it is difficult to determine when the AFM probe first comes into contact with the soft cell surface (24). Hence, it is difficult to determine how much the cell is deformed during the measurement and to measure the cell topography without any deformation. To reduce the forces on the cell surface and to have a probe of defined geometry a bead of 1–30 μm diameter is often attached to the AFM cantilever (for example see Lu et al. (17)). This, however, reduces the spatial resolution. We present, to our knowledge, the basis of a new method that can be carried out with submicrometer spatial resolution and where the force is applied without there ever being contact of the probe with the cell surface. We then explore its use to measure the mechanical properties of a range of cell types.

Submitted January 28, 2008, and accepted for publication May 6, 2008.

Daniel Sánchez, Nick Johnson, Chao Li, Pavel Novak, and Johannes Rheinlaender contributed equally to this work.

Address reprint requests to Yuri E. Korchev, Division of Medicine, Imperial College London, Hammersmith Hospital Campus, Du Cane Road, London, W12 0NN, UK. Tel.: 44-0-2083833080; Fax: 44-0-2083838306; E-mail: y.korchev@imperial.ac.uk.

Daniel Sánchez's present address is Cinvestav-Unidad Monterrey, Av. Cerro de las Mitras 2565, Col. Obispado, C.P.64060. Monterrey, Nuevo León, Mexico.

Yanjung Zhang's present address is China National Academy of Nanotechnology and Engineering, Tianjin, China 300457.

Christopher Benham's present address is Dept. of Life Sciences, University of Hertfordshire, Hatfield, Herts AL10 9AB, UK.

Editor: Richard E. Waugh.

0006-3495/08/09/3017/11 $2.00

doi: 10.1529/biophysj.108.129551

Our method is based on scanning ion conductance microscopy (ICM), that uses a pipette as the probe (25–30). The technique uses the ion current flowing through a pipette to control the pipette-surface separation (31,32). With the pipette in the bath, the ion current is limited initially by the resistance of the pipette. However, as the pipette approaches the surface, reducing the separation, the ion current reduces further. This reduction is used for distance feed-back control, and is set at ~1%, i.e., the current is 99% of its maximum value. This means the pipette is controlled over the surface at a separation of about one pipette inner radius. This system has provided high resolution noncontact imaging of a number of different living cells and has followed structural rearrangements of the cell membrane (25–29) and followed cardiac myocyte contraction (30).

No hydrostatic pressure is applied through the pipette during imaging of topography, but a major facility of our system is that pressure can conveniently be applied through the same scanning pipette probe to study the mechanical properties of the cell. Fig. 1 *A*, schematically outlines the system and depicts the membrane deformation (Fig. 1 *B*) during hydrostatic pressure changes (0.1–150 kPa) applied via the pressure port to the cell surface. The deformation of cell surface invokes the distance feedback control, adjusting the pipette position to keep the reduction in ion current constant. The pipette's position, *h*, is thus a function of applied pressure and the mechanical properties of the local cell surface underneath the pipette, and we can, noninvasively, locally indent or evert the cell surface. First, we carried out experiments on model samples of known mechanical properties to quantify the force exerted on the sample on the application of pressure. We then validated our method by applying it to a red blood cell and then applied it to epithelial cells, cardiomyocytes, and neurons.

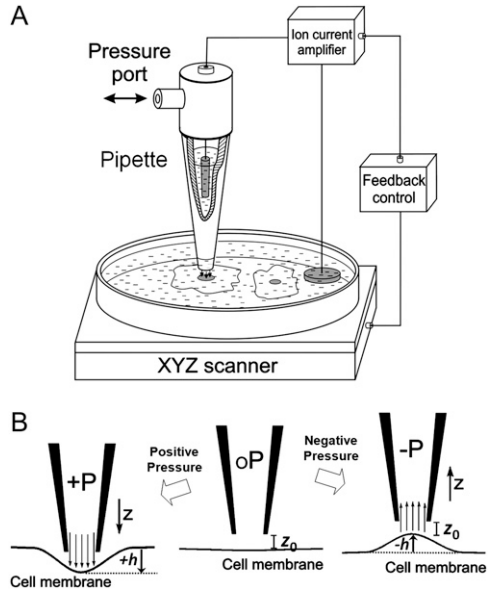

FIGURE 1 Noncontact mechanical stimulation by the scanning ICM. (*A*) Schematic diagram of the ICM. While the pipette scans the cell membrane, the ICM feedback control system uses the ion current between the bath and pipette electrodes to keep the pipette-surface distance, z_0, constant. (*B*) Positive or negative hydrostatic pressure is noninvasively applied to the cell surface via the pressure port. Consequent deformation of the cell surface invokes the distance feedback control to adjust the pipette position, to keep z_0 constant and the change in pipette position, *h*, is measured and recorded.

MATERIALS AND METHODS

Scanning ICM microscopy

These experiments were carried out using a scanning ICM (Ionoscope Limited, London, UK) as described previously (30). Briefly, the ICM uses a pipette as a scanning probe arranged perpendicularly to the sample, mounted on a three-axis piezo translation stage. The scanning ICM feedback control system keeps the ion current through the pipette constant to approach and scan over cells, while maintaining a constant separation distance of approximately the pipette internal radius from the cell surface. This is done by modulating the pipette sample separation and using the resultant ac signal normalized by the dc current for distance feedback control. The frequency of the modulation used was 200 Hz, so the feedback is significantly faster than the rate of pressure application in these experiments, ~0.1 Hz. The currents in these experiments were in the range 0.5–10 nA. These currents flow between the electrodes in the pipette and in the bath. As we have shown previously, ion channel activity does not affect the distance feedback control, because the current generated by an ion channel opening is several orders of magnitude smaller than the current passing through the pipette. Likewise, there is no voltage drop across the cell membrane that could trigger ion channel activity (see Supplementary Material in Shevchuk et al. (29)). The scanning ICM produces a 3D topographical image of the cell membrane during scanning, and then the pipette can be moved accurately to an area or a specific structure of interest. To apply hydrostatic pressure, the pipette was mounted in a patch-clamp electrode holder (Harvard Apparatus, Kent, UK). Positive or negative hydrostatic pressure can be locally supplied through the pressure port of this holder via tubing and a syringe. In our initial experiments the syringe was moved manually and the pressure was recorded using a PM100D pressure manometer (World Precision Instruments, Stevenage, UK). In later experiments the syringe was moved using a dc motor that allowed more reproducible changes in applied pressure. The applied pressure was digitally recorded along with corresponding changes in the pipette position that occur while ICM distance feedback followed the resulting local movements of the cell surface. All experiments were carried out at 20°C.

The ICM nanopipettes were pulled from borosilicate glass capillaries (Intrafil, 1.0 mm OD × 0.58 mm ID; Intracel Ltd, Hertz, UK), using a laser-based electrode puller (P-2000, Sutter Instrument, Novato, CA). The half cone angle of the pipettes was 1.5–3°. The preparation of the cells used in this study is described in Supplementary Material, Data S1. The pipettes that were used to carry out the mechanical stimulation to living cells had an electrical resistance of 13–25 MΩ when submerged in the L15 medium.

Materials

Rectangular AFM cantilevers, 100 um long and 30 um wide were used for calibrating the force exerted by the pipette (BioLever, Asylum Research, Santa Barbara, CA). Their spring constants were measured using the thermal noise method (33) as $k = 5.4 \pm 0.5$ nN μm^{-1}. For the pressure experiments, the cantilevers were oriented with the tip pointing away from the pipette. A Triangular 320-μm Microlever Probe (Veeco Instruments, Cambridge, UK) with a nominal spring constant of 0.01 Nm^{-1} was used for the experiment to determine the dependence of the applied force with pipette radius.

Decane (Sigma-Aldrich, Steinheim, Germany) was dabbed on a clean petri dish using a borosilicate glass capillary. NaCl phosphate buffer solution

(150 mM) containing 1 mM NaN_3, 10 mM Na_2HPO_4, pH 7.2 was pipetted into the dish, and small decane drops remained adhered to the dish surface. Sodium dodecyl sulphate (BDH Laboratory Supplies, Poole, UK) was added to achieve the desired concentrations.

Modeling

Theoretical calculations of the fluid flow through a nanopipette were carried out using finite element modeling (FEM). The incompressible Navier-Stokes equation was solved using COMSOL Multiphysics software (version 3.3, FEMLAB GmbH, Goettingen) with the fluid dynamics module. The model geometry was axially symmetric and consisted of the interior of a conical pipette (axial length $L = 1$ mm, half cone angle $\theta = 3°$) and of the exterior fluid volume above a flat sample surface (5 μm in axial and 5 μm in radial direction). The boundary conditions were ''normal flow'' and ''normal pressure'' at the pipette backside opening, ''neutral'' at the model borders at the volume above the sample and ''no-slip'' at the pipette walls and on the sample surface. The FEM mesh was refined three times, consisted of 14,912 triangular elements and 69,727 degrees of freedom, and was solved with the direct (UMFPACK) linear solver (solving time ~20 s). The density of the fluid was assumed as $\rho = 10^3$ kg/m^3 and the viscosity as $\eta = 10^{-3}$ Pa s.

RESULTS AND DISCUSSION

Calibration of force exerted via the pipette

First we calibrated the ICM using an AFM cantilever with measured spring constant of 0.0054 Nm^{-1} using pipettes with radii 100–1000 nm positioned at the tip of the cantilever. The pipette inner radius, r_i, can be estimated from the formula published previously (34);

$$R_{\text{pipette}} = \frac{1}{\pi \xi r_i \tan\theta}, \quad (1)$$

where R_{pipette} is the pipette resistance, θ is the half cone angle of the inner wall of the pipette and ξ is the conductance of the solution. This formula assumes that the access resistance, which depends on the pipette geometry, is zero. The access resistance contribution to R_{pipette} was found to be $<4\%$, so this assumption is valid. The formula was verified experimentally using scanning electron microscopy for small pipettes or optical microscopy for the pipettes of large diameters (data not shown). Increasing the hydrostatic pressure applied to the pipette increases the force on the cantilever so it bends, and we can monitor this by measuring the corresponding change in pipette position, h, because the distance feedback control adjusts the pipette position to keep constant separation, z_0, between the pipette and the cantilever as shown in Fig. 1. Fig. 2 *B* shows the change in applied pressure with time and the corresponding change in the position of the tip of the cantilever. Control experiments over a glass coverslip showed no detectable change in pipette position with applied hydrostatic pressure (data not shown). Because the control signal for ICM feedback is normalized by the dc current, we also detected no change in pipette position over glass when increasing the applied voltage. When the same experiment was carried out over the cantilever, we also observed no change in position with voltage showing that there are negligible forces exerted by the electro-osmotic flow without the application of hydrostatic pressure (data not shown). This was confirmed by the observation that we obtained identical pressure-displacement curves (as the one shown on Fig. 2 *D*) with positive and negative voltage that reverses the direction of electro-osmotic flow (data not shown).

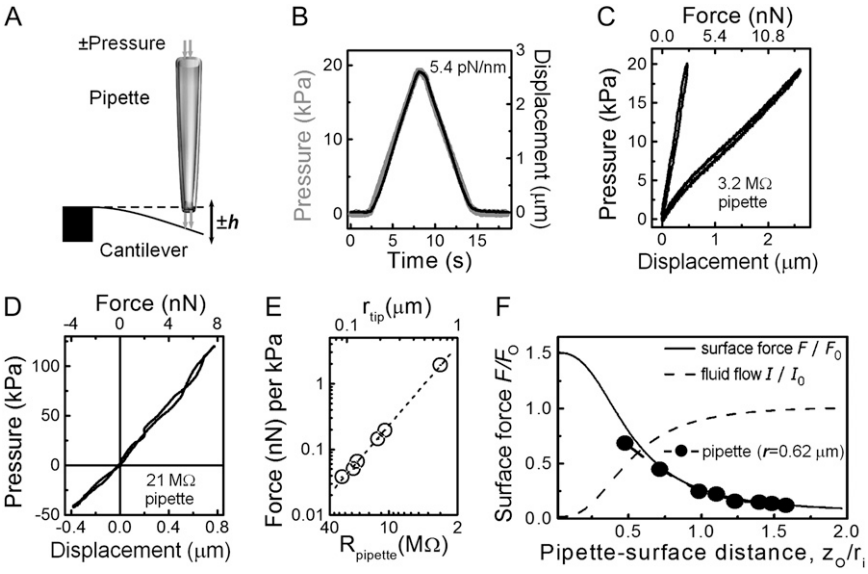

FIGURE 2 Force calibration. (*A*) Schematic of the calibration of the force exerted by the pipette on a cantilever with the application of hydrostatic pressure. (*B*) Graph of a triangular pressure pulse (applied via the pipette) with time. Pressure bends the cantilever tip (spring constant 0.0054 Nm^{-1}), and the system measures the pipette's position, h. (*C*) Linear relationship between the distance and pressure, using pipette with 3.2 MΩ resistance for z_0 of 310 nm (*steeper line*) and 900 nm (*flatter line*). (*D*) Plot of the pressure versus the exerted force and the cantilever displacement using a 21 MΩ pipette. This shows a linear dependence like in *C* and also that negative pressure bends the cantilever in the opposite direction. (*E*) Calibration curve of pressure/force versus the pipette resistance and pipette radius for a fixed pipette-sample separation of half the inner radius. (*F*) Plot of F/F$_0$, the ratio of the force on the cantilever to F$_0$, the force given by $\Delta P\ \pi r_i^2$, as a function of the pipette-surface separation maintained by the distance feedback control during the pressure ramps. The calculation of the force and fluid flow from finite element modeling are also shown for comparison (*solid* and *dashed line*, respectively). For the modeling, $r_i = 1\ \mu$m, $r_o = 1.5\ \mu$m, $\theta = 3°$, $\Delta p = 100$ kPa, and $\eta = 1$ mPa s.

The relationship between the cantilever displacement and applied pressure was linear, with no hysteresis (Fig. 2 *C*). However as shown in Fig. 2 *C* the force exerted depended on z_0 and the exerted force increased when z_0 was reduced. It is also possible to apply negative pressure and deform the cantilever in the opposite direction (Fig. 2 *D*). We made a series of measurements with the same pipette. The pressure was ramped and the deformation of the cantilever measured, with the distance feedback maintaining different values of z_0, up to a separation where distance feedback control became unreliable. We obtained the dependence for the force applied to the cantilever with z_0, the pipette-surface distance maintained by the distance feedback control, as shown in Fig. 2 *F*.

Modeling

To investigate the observed distance-dependence of the force on the cantilever in Fig. 2 *F* we modeled the fluid dynamics inside and just outside the pipette tip. The fluid flow through the pipette can be calculated analytically. Based on the Hagen-Poiseuille law the equation relating the flow I_0 through a pipette to the pressure drop ΔP over the pipette is:

$$I_o = \frac{3\pi \tan\theta}{8\eta} r_i^3 \Delta P, \tag{2}$$

where ΔP is the hydrostatic pressure difference applied between the pipette backside opening and the bulk liquid, r_i is the inner opening radius of the pipette tip, θ is the half cone angle of the inner wall of the pipette, and η is the viscosity of the fluid. Note that I_0 is independent of pipette length (for $L \gg r_i$). For example, $r_i = 1$ μm, $\theta = 3°$, $\eta =$ 1 mPa s (water), and $\Delta P = 100$ kPa results in a flow of $I_0 = 6 \times 10^{-12}$ m^3/s $= 6$ nL/s. For a nonzero flow through the pipette, the pressure in the pipette decreases toward the tip.

To obtain the force exerted onto a flat, undeformable sample, like the cantilever, as a function of tip-surface separation, z_0, we modeled the fluid flow in the pipette and in the tip region in vicinity to the surface with finite element modeling (FEM). The pipette is taken as tapered with a half cone angle $\theta = 3°$, an inner opening radius $r_i = 1$ μm, an outer radius $r_o = 1.5\, r_i$ and a length of 1 mm. At the backside opening of the pipette a pressure of 100 kPa is applied. The walls of the pipette and the sample surface are defined as ''no-slip'', which means fluid velocity is zero there. From the FEM model we obtain the distribution of the hydrodynamic pressure (Fig. 3 *B*). The hydrodynamic pressure at the sample surface varies both laterally and with the pipette vertical position. For example, with $z_0 = 0.5$ μm the maximum pressure on the sample surface is ≈50 kPa, about half of the applied pressure. Laterally, it is about constant for $|r| < r_i$ and decreases approximately linearly to almost zero at $|r| = r_o$. The flow is laminar and the distribution of the flow velocity is shown in Fig. 3 *A*. The pipette length modeled here is more than sufficient, because the dominant viscous effects occur in the lower narrow tip of the pipette. Also, the size of the outer

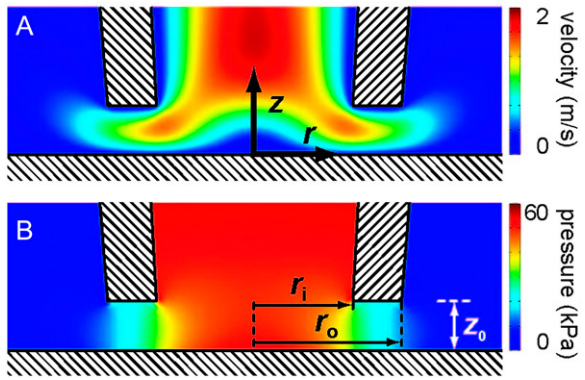

FIGURE 3 Finite element modeling. Pressure distribution (*A*) and absolute value of fluid velocity (*B*) of viscous fluid flow through a pipette in close proximity to a flat sample surface ($r_i = 1$ μm, $r_o = 1.5$ μm, $\theta = 3°$, $z_0 = 0.5$ μm, $\eta = 1$ mPa s, $\Delta P = 100$ kPa).

fluid domain modeled is sufficiently large, because the pressure and fluid velocity drop quickly at increasing distances from the contact region (Fig. 3).

The flow at the pipette is dominated by viscous forces (corresponding to low Reynolds numbers). Therefore, the acting forces can be obtained directly from the axially symmetric pressure distribution $P(r)$ (Fig. 3 *B*). Thus, the total normal force on a flat, undeformable sample surface can be obtained by integration over the radius r:

$$F = 2\pi \int_0^\infty P(r)\, r dr. \tag{3}$$

From several FEM calculations with varying z_0 we obtained the force exerted on the cantilever (Fig. 2 *F*, *solid line*) and the fluid flow (Fig. 2 *F*, *dashed line*) as a function of pipette-surface distance. The force becomes maximal when approaching zero distance ($z_0 \to 0$) because the flow becomes infinitesimally small and no pressure drops over the pipette due to viscous friction at its walls. At small pipette-surface distances the total force is larger than simply pressure multiplied by pipette opening area $F_0 = \Delta P\, \pi r_i^2 = 0.31$ μN, because of nonzero pressure underneath the pipette walls at $r_i < |r| < r_o$. As the pipette-surface distance increases, fluid flow increases, and because the pressure drop over the pipette rises proportionally to the flow (Eq. 2), the pressure reaching the tip and therefore the force exerted on the sample surface decreases. At large pipette-sample-distances ($z_0 \to \infty$), the flow I approaches the saturation value $I_0 = 6$ nl/s given by Eq. 1. Note that the force does not approach zero for $z_0 \to \infty$ but remains at ≈1% of F_0 due to inertial effects as the Reynolds number is small but nevertheless larger than zero. This calculation matches the experimental data on the cantilever very well as shown in Fig. 2 *F*.

We can also use this model to estimate the shear stress (shear force per unit area) exerted on the surface. The shear stress is given by the viscosity, η, multiplied by the derivative with respect to z of the velocity component tangential to the surface, dv_r/dz:

$$F/A = \eta \, dv_r/dz. \quad (4)$$

From the calculated velocity field (Fig. 3 *A*) it can be seen that the shear stress is zero centrally below the pipette. It is maximal at $r = r_i$ where $dv_r/dz = 12\ s^{-1}$, yielding a maximum shear stress of 12 nN/μm^2.

Force generated on a deformable surface

We next carried out experiments on oil droplets of decane, as a model of a cell surface that can be deformed on application of pressure. This surface has a known surface tension of 0.05 N m^{-1} giving a spring constant, k_0 of 0.062 N m^{-1} (35) allowing us to directly quantify the force we exert on a soft deformable surface using the pipette and how this depends on the pipette-sample separation, z_0. Typical data are shown in Fig. 4 *B*, again showing a linear dependence of deformation with applied pressure. Assuming the force applied by the pipette is given by $\Delta P\ \pi r_i^2$, the data in Fig. 4 *B* can be used to determine the apparent spring constant of the surface, k. Similarly to the case of the cantilever we observed that smaller pipette-sample-separations, z_0, result in larger sample deformations/deflections and larger values of k/k_0 (Fig. 4 *C*). When k/k_0 equal one, the applied force must actually be equal to $\Delta P\ \pi r_i^2$. This occurred at greater separations from the surface than for the AFM cantilever; 0.4 r_i for the cantilever (Fig. 2 *F*) compared with ~1.1 r_i for the oil droplet (Fig. 4 *C*). Presumably this is because deformation of the droplet decreases the flow and hence increases the pressure at the surface. This experiment shows that, when the pipette is controlled above the surface with a separation z_0 of 1.1*ri*, the force developed at the surface is equal to $\Delta P\ \pi r_i^2$; and if a different separation is used, then the data in Fig. 4 *C* can be used to determine a correction factor. Note that above a critical force the dimple formed in the surface of the oil droplet collapses due to the force applied via the pipette, as shown previously (36). This occurs approximately when the dimple has a radius of r_0 so the pressure required is $2\gamma/r_0$. This collapse means that it is not possible to apply pressure ramps when the pipette is too close to the surface and limits measurements to larger separations and also limits the maximum pressure that can be applied.

Repeated experiments ($n = 14$) on decane oil droplets, with the value of z_0 kept at 1.1 $r_{i,}$ gave a mean value for the spring constant of 0.065 ± 0.040 N m^{-1}. The mean value is close to the value measured by AFM (35) showing the accuracy of the method. The major source of the variation is probably variation in the shape of the pipette tip, so that the inner pipette radius is not exactly inversely proportional to the pipette resistance as stated by Eq. 1. Because the application of pressure is under computer control it is also possible to systematically change the rate of pressure application. Experiments on decane showed no variation in the measured surface tension with rate of pressure application from 1.4–10.9 kPa s^{-1} (data not shown).

We then measured the spring constant of a decane oil droplet in the presence of 10 mM of the surfactant sodium dodecyl sulfate (SDS), which will reduce the spring constant, k_0, to 0.012 N m^{-1} (35). Representative results show the same linear dependence as in the absence of SDS (Fig. 4 *B*). As shown in Fig. 4 *C* the functional dependence of the apparent spring constant with pipette-sample separation, z_0, was similar in the presence and absence of SDS. These are the same within the experimental error in estimating the pipette inner radius from the pipette resistance. Importantly in both cases we find that the apparent spring constant at the normal control distance of an inner radius is close to the measured value. These results show that over a deformable surface the pipette only needs to be an inner radius away from the surface before the full pressure is developed at the surface, so that the applied force is then equal to $\Delta P\ \pi r_i^2$. The main error in the application of this equation is the estimate of the pipette radius from the pipette resistance.

Pressure response of red blood cells

Having established the quantitative relationship between pressure applied to the pipette and the force exerted for pipettes of different resistances, we then measured the mechanical response of a red blood cell, as diagrammed in Fig.

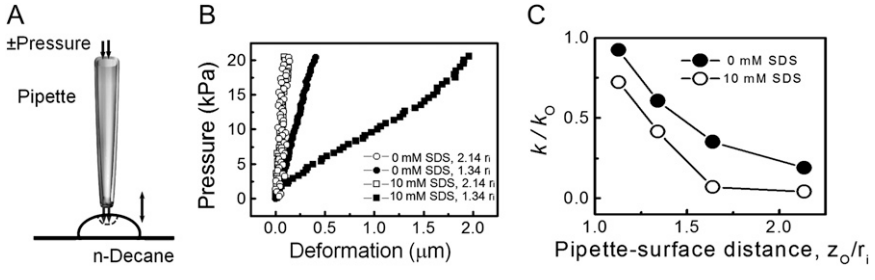

FIGURE 4 (*A*) Schematic of the experiment. (*B*) Representative data from an experiment measuring the deformation of the oil droplet with pressure at different values of z_0 in the absence and in the presence of 10 mM SDS. (*C*) Ratio of the apparent spring constant, k, to the real spring constant, $k_{0,}$ when pressure is applied to a pipette at different normalized separations n, z_0/r_i, from the surface of a decane droplet. The experiment was carried out under salt solution with and without 10 mM SDS and r_i was 0.75 μm. k is calculated assuming the force exerted on the droplet is given by $\Delta P\ \pi r_i^2$. It is not possible to make measurements with a separation smaller than a pipette radius due to collapse of the dimple in the surface of the oil droplet.

5 *A*. The mechanical response of red blood cells has been measured by AFM, allowing direct comparison with our results. Fig. 5 *B* shows a typical experiment where a pressure ramp is applied to the cell, via the pipette, and the deformation this produces was measured by monitoring the position of the pipette. This was done under distance-feedback control so that constant separation, z_0, is maintained between the pipette and cell surface during the experiment and the cell cannot contact the pipette. The cell deforms linearly with applied pressure. It returns to prepressure position, on pressure reduction (data not shown) and hysteresis was observed in many cases. Fig. 5 *C* plots pressure versus deformation. Because we are controlling at the pipette inner radius over a soft deformable surface we assume that the full pressure, ΔP, is developed at the surface over a circular region of radius r_i, as we found on the oil droplets. Johnson (37) has shown that for uniform pressure, ΔP, applied over a circular region of radius r_i on a flat, semi-infinite elastic half space the vertical displacements $h(r)$ are given by:

$$h(r) = \frac{4(1-\nu^2)r_i\Delta P}{\pi E}\mathbf{E}(r/r_i) \quad (r < r_i), \tag{5}$$

where ν is the Poisson ratio and E is the modulus of elasticity (Young's modulus) and $\mathbf{E}(r/r_i)$ is the complete elliptic integral of the second kind evaluated at r/r_i. The displacement at the center of the region is $2(1-\nu^2)\, r_i\, \Delta P/E$ whereas it is smaller at the edge, $4(1-\nu^2)\, r_i\, \Delta P/(\pi E)$. The average displacement of the circular region, h_{avg}, assumed to be the distance measured by the pipette, is given by

$$h_{avg} = 16(1-\nu^2)r_i\Delta P/(3\pi E). \tag{6}$$

Thus the gradient of pressure versus distance, which should be a straight line, can be used to calculate E. Assuming an incompressible material and small strains then ν is 0.5. Therefore the example in Fig. 5 *B* gives an apparent Young's modulus of 4.2 kPa. This is referred to as an apparent Young's modulus because the assumption of a homogeneous elastic planar substrate is clearly not the case for a cell. The average of 20 measurements gives an apparent Young's modulus of 4.4 ± 0.6 kPa ($n = 20$), in good agreement with the literature values of 4.9 ± 0.5 kPa (19) and 4 kPa (38). This result validates the use of this method for the noncontact measurement of mechanical properties of cells.

Mechanical properties of epithelial cells

We then studied the mechanical properties of a range of different cells. The response of the cell depends on both the rate of application of force and the extent of deformation. In all these experiments we used slow pressure ramps, around 0.1 Hz so that the probe velocity is around 0.1 μm s^{-1}, so as to obtain high signal/noise data and allow comparison between different cells and because, under these conditions, cells have shown to be most elastic (17,39). Higher rates of force application generally lead to increased viscoelastic behavior. This means that initial deformation of the cell was carried out under rates of deformation that allow comparison with AFM studies reported previously.

First, we studied the mechanical properties of epithelial cells because these cells are required to resist mechanical forces. A6 toad epithelium kidney cells were grown on filters in a confluent layer (Fig. 6 *A*). A typical plot for mechanical probing of these cells is shown in Fig. 6 *B*. The live cell appears soft initially, at low applied pressure, and then is more resistant as the size of the deformation increases. We found that the cell shows hysteresis—the return to its original position is slower and typically took up to 10 min and was observed to return to its original position in at least 30 cases. The data can be analyzed in an identical way to the red blood cell to obtain the apparent Young's moduli. We found that the cell has an initial apparent Young's modulus of 4.5 kPa, increasing to 7.8 kPa after deformations of 750 nm (Fig. 6 *D*). These values are in agreement with previous reports on Madin-Darby canine kidney epithelial cells where the Young's modulus was 5–7 kPa (40).

High resolution scanning ion conductance microscopy (SICM) imaging of A6 cells (27) shows that fixation leads to reductions in the cell height. At the same time, the lateral dimensions of the cells change very little due to the attachment of the cells to the surface and adjacent cells. We found that the pipette moves down by ~2.5 μm when the A6 cells are fixed (Fig. 6 *C*), confirming that the cell has shrunk vertically. Fixation also makes the cell significantly harder. The mechanical behavior of the fixed cell is also very different. A fixed cell has an initial high apparent Young's modulus of 800 kPa at small displacements, which then decreases to 80 kPa at larger displacements (Fig. 6 *E*), suggesting some breakdown or yielding of a mechanical

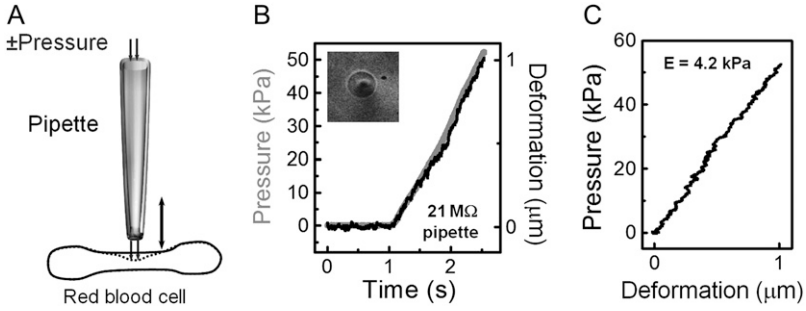

FIGURE 5 Red blood cell response to pressure. (*A*) Schematic diagram of the calibration of the force exerted by the pipette on a red blood cell. (*B*) Plot of applied pressure and resulting cell deformation with time. Only data with increasing pressure are shown. The cell deforms linearly as pressure is applied. (*Inset*) Phase contrast image of the red blood cell. The black-dot in the center is the position of the tip of a 21 MΩ resistance pipette. (*C*) Plot of pressure versus distance, from the experiment in *B*.

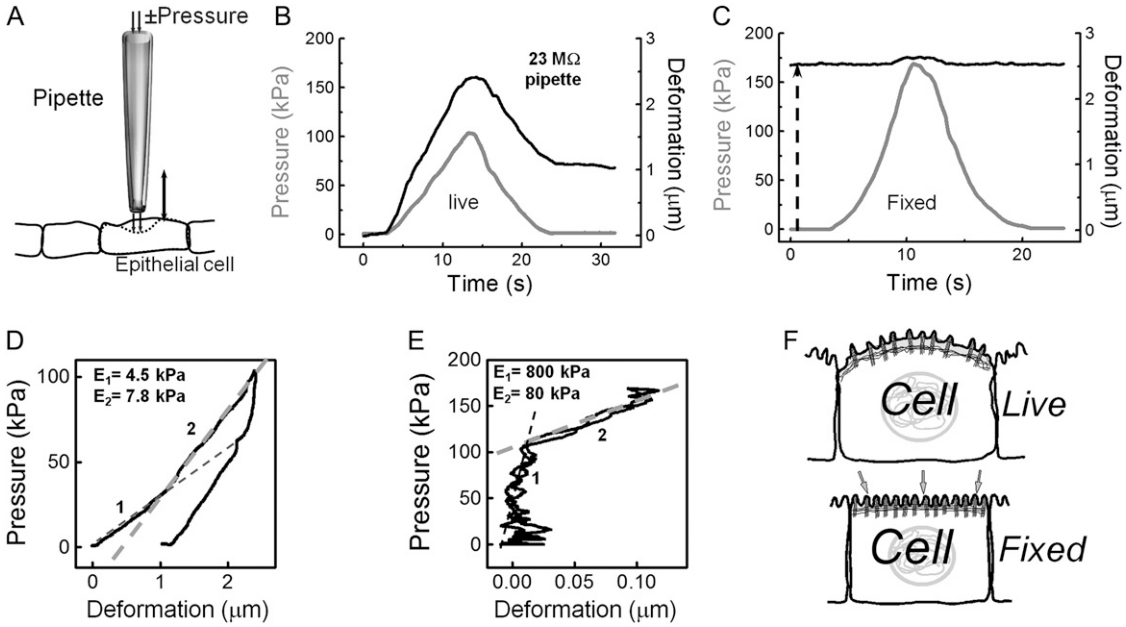

FIGURE 6 Epithelial cell response to applied pressure. (*A*) Schematic diagram. (*B*) Plot of applied pressure and resulting deformation distance with time. (*C*) Same experiment on the same cell as in *B* but with the cell now fixed. The data are presented on the same scale for comparison. (*D*) Pressure-deformation curves for the live cell experiment in *B*. (*E*) Pressure-deformation curves for the fixed cell experiment in *C*. (*F*) Schematic diagram showing changes with fixation.

structure. Fixation clearly results in the cell surface shrinking and becoming more rigid, as flexible structures are locked in place as illustrated in Fig. 3 *F*. A similar hardening of red blood cells (15) and kidney cells (41) with fixation has been found with AFM. In live cells the mechanical response of the cell membrane shows a relatively low Young's modulus for small indentations. With further indentation the Young's modulus increases possibly due to the membrane interacting more strongly with the underlying cytoskeleton. A prominent hysteresis (Fig. 6 *D*) is probably due to the slow breaking of the interactions between the plasma membrane and underlying cytoskeleton that may well involve an active cellular process over the 10 min recovery period.

There are independent data supporting this suggestion. The stiffness of kidney epithelial cells has been studied as the osmolarity of the solution is changed (41). Hypertonic solution led to the cell shrinking in size and the Young's modulus increasing as the cell membrane collapsed onto the cytoskeleton. Hypotonic solution led to the cell swelling and the Young's modulus decreasing due to detachment of the cell membrane from the cytoskeleton. Furthermore, Pesen and Hoh (22) have also interpreted their mechanical measurements of endothelial cells as a soft region of a few hundred nanometers over an intertwined fine and coarse cortical mesh that is consistent with the model presented here.

Mechanical properties of cardiomyocytes

We then studied rat cardiomyocytes under conditions where there were no spontaneous contractions (see Data S1 for details). With zero applied pressure, we have previously produced SICM images showing that cardiomyocytes have repetitive scalloped topographic features (42), as shown in Fig. 7, *A* and *B*. On application of pressure, the cell indents with clear differences between the first 200 nm of deformation and the following larger indentations (Fig. 7, *C* and *D*). The average of 10 experiments shows that the initial apparent Young's modulus is 1.4 kPa and a later apparent Young's modulus of 3.0 kPa (Fig. 7 *E*). Note that the scallop region is still relatively flat with a vertical dimension of ~0.2 μm compared with a lateral dimension of 2 μm, so the two different apparent Young's moduli are probably related to the internal structure of the cell. The initial deformation may also involve the mitochondria just under the cell membrane. These values obtained are lower than those previously reported for rat cardiomyocytes, around 30 kPa (18). This may reflect differences in the tip size used, the state of the cells because more physiological conditions were used in this study, and the loading rates. In previous work the lowest probe velocity used was 0.6 μms^{-1} whereas in our studies it is significantly slower.

We have shown previously that ICM can be used to measure cardiomyocyte contraction (30). Here we have shown that pressure applied via the pipette can mechanically stimulate contraction of the cardiomyocyte that can be detected by both optical microscopy and ICM (Movie S1). The method seems to have potential to probe mechanosensitivity in detail, without cell contact, by applying controlled forces, and will be studied in more detail in a future study. This method would build on our previous work where we stimulated neurons, without contact, by application of pressure (43). We now know and can control the magnitude of the

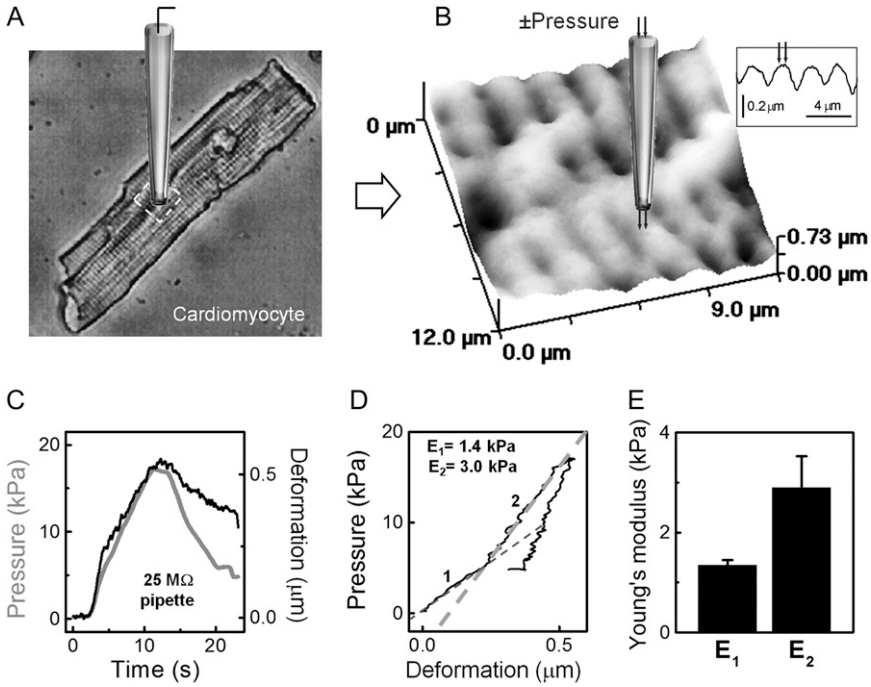

FIGURE 7 Mechanical properties of rat cardiomyocytes. (*A*) A phase contrast image of the used rat cardiomyocyte with diagrammed pipette. (*B*) ICM image of the dotted-square region of cardiomyocyte marked in the phase contrast image *A*. Repetitive topographic scallop features are locally probed to measure their mechanical properties. (*C*) Plot of applied pressure and resulting cardiomyocyte deformation with time. (*D*) Plot of pressure versus deformation, from experiment in *C*. The curves have two linear gradients (1 and 2). (*E*) Young's modulus (elastic modulus) E1 and E2 of the two components (1 and 2) in *D*. Bars = mean ± SD of 10 experiments.

applied force. This work could be extended to map the locations of mechanosensitive ion channels, in a similar fashion to that used to map ATP dependent K^+ channels (44). The probe would apply local pressure (instead of K^+) while scanning the cell surface. A second patch pipette measures changes in whole cell currents as the probe scans over and activates a mechanosensitive channel. AFM probes have been used previously to activate cells by local application of force and detection of activation by measurement of increased intracellular calcium (45). Our method, however, has the advantage that the force is applied without contact with the cell surface, allowing the whole cell surface to be scanned.

Pressure response of neurons

We applied our method to a ''softer'' cell, by probing the body of cultured rat dorsal root ganglion (DRG) sensory neurons using both positive pressure (Fig. 8 *A*) and negative pressure (mild suction) (Fig. 8 *B*). Fig. 8 *C* shows the pressure versus distance curves with two different linear gradients. The softer initial gradient, shown by the thin dotted line, gives an apparent Young's modulus, E_1, of 0.5 kPa whereas the later, harder gradient gives an apparent Young's modulus, E_2, of 6.9 kPa. Negative pressure gives a similar soft apparent Young's modulus, E−, of 0.4 kPa. We then carried out the same experiment at four different positions on the cell surface as shown in Fig. 8 *D*. Fig. 8 *E* shows the result of 20 such experiments. The apparent Young's moduli with suction was the same as the initial apparent Young's modulus measured with positive pressure, within experimental error. At larger deformations, a second higher apparent Young's modulus was measured. The initial value we have measured is in good agreement with that measured by AFM on neurons, around 0.48 kPa at the lowest loading rates used. These experiments also showed that the Poisson ratio was close to 0.5 (17). However, the AFM experiments used only small deformations that were limited to a fraction of the radius of the bead attached to the AFM cantilever (~3 μm). Therefore, the higher Young's modulus was not observed. Our interpretation of the two different apparent Young's moduli obtained by the ICM technique is that with an indentation of about a micrometer, resistance increases when the membrane encounters additional interactions with the underlying cytoskeleton and/or the nucleus. As shown schematically in Fig. 8 *F*, there appears a submembrane space of about a micrometer where there are few interactions between the cell membrane and cytoskeleton that gives rise to the initial low apparent Young's modulus. The apparent Young's modulus then increases by about an order of magnitude as the cell is deformed to a greater extent. There can be a contribution to the measured Young's modulus from the harder underlying substrate (46,47). This should result in a smooth increase in apparent Young's modulus with deformation, unlike the sudden change we observe here. Furthermore, the sudden order of magnitude increase we observe occurs at deformations of only 10–20% of the initial cell height and was much greater than predicted if it was due to a substrate contribution alone (46,47). This sudden large increase in Young's modulus is caused when the underlying cytoskeleton or the nucleus is encountered. Further experiments are clearly required to test this interpretation but we note that a great deal of the studies of cell structure have been carried out on fixed cells where the shrinkage of the membrane would make any submembrane space undetectable.

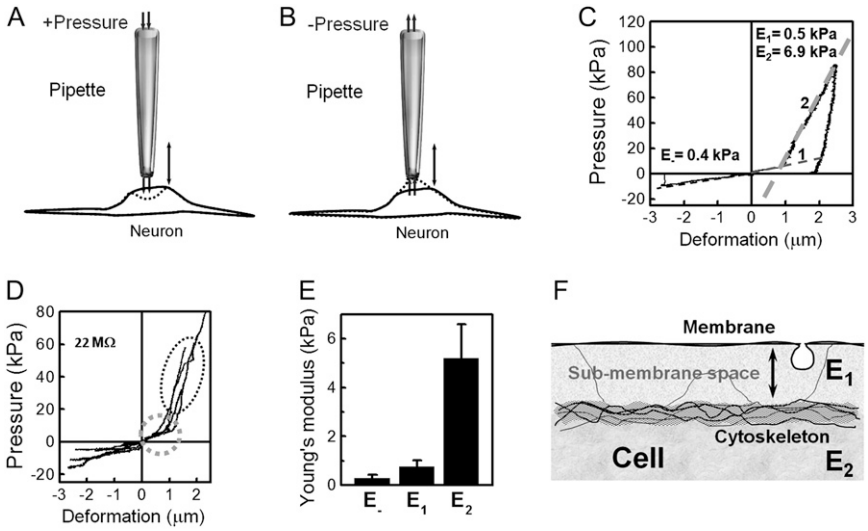

FIGURE 8 Pressure response of DRG neurons. (*A*) Schematic diagram of experiments to measure the mechanical response of a DRG neuron with positive pressure applied and by applying negative pressure (suction) as shown in *B*. (*C*) Representative plot of pressure versus deformation for the experiments in *A* and *B*. The curves show Young's modulus with $E- = 0.4$ kPa, for the negative pressure, and with two linear components with different gradients $E_1 = 0.5$ kPa and $E_2 = 6.9$ kPa for the positive pressure. (*D*) Pressure-deformation experiments with increasing pressure carried out at four different positions on the neuron body showing the reproducibility of the experiment. (*E*) Histograms of 20 experiments comparing the Young's modulus E-, E_1, and E_2. Error bars = 1 SD. (*F*) Schematic diagram showing the presence of a submembrane space above the cytoskeleton that explains the different values of Young's modulus for E_1 and E_2.

These results indicate that our method can exert sufficiently small forces to resolve the mechanical properties of the different mechanical elements that make up the cell. This has an advantage over other methods, such as AFM, that require contact with the cell surface to exert force, and hence there must always be a significant, albeit small, initial force applied at the start of measurement and therefore the soft cell surface may be predeformed before the start of the measurement. As we have shown in this work, larger deformations are possible, without contact with the cell, allowing us to probe the underlying cytoskeleton. In addition, because the pipette never touches the cell surface, it does not get contaminated, and repeated experiments are possible at different positions on the cell surface in one experiment. Typically, one pipette can be used for at least several hours before it needs replacing, due to fouling as detected by a change in pipette resistance. In future work, we can use this method to explore the cellular response in more detail by changing the rate of applied pressure and the use of drugs to prevent actin polymerization or depolymerize the already formed actin cytoskeleton. This work can be straightforwardly extended to mapping of the mechanical properties by carrying out a series of point measurements at different positions or scanning the cell first with no applied pressure, and then with fixed pressure applied to the pipette, and subtracting the two images. Mapping and characterization of mechanosensitive ion channels is also possible without contact with the cell. We have shown that the force exerted by the pipette, when controlled at the inner radius from the surface is given by $\Delta P\ \pi r_i^2$, so that the method relies on an accurate estimate of the pipette radius. This formula will be valid only on flat regions of the cell surface, as studied here. However, on convoluted regions the assumption that the force developed at the cell surface is equal to $\Delta P\ \pi r_i^2$ and that Eq. 6 can be used to determine the apparent Young's modulus may be inaccurate. The future extension of the FEM simulations to a soft deformable surface of different shapes would be a great help in determining how the exerted force depends on the sample topography and how this in turn modifies Eq. 6. Because the SICM can directly determine the undeformed cell topography, before the application of pressure, it should then be possible to correct for cell topography and more accurately determine both the applied force and the Young's modulus. However, whenever the surface topographic features are much smaller than the pipette-surface distance, their influence is small because the velocity of the fluid approaches zero at the surface. Thus small surface features do not alter the fluid flow and therefore do not affect the vertical force that is exerted on the surface. One last point is that the dependence of the applied force on the square of the pipette inner radius sets a limit to the possible resolution of any mechanical maps of the cell surface because there is a limit to the pressure that can be applied via the pipette. This limit is in the range of 100–300 nm depending on the mechanical properties of the cell.

We have studied three distinct classes of cells—epithelial cells, cardiomyocytes, and neurons—and found that on applying increasing force to the cell surface, the calculated initial modulus of elasticity (apparent Young's modulus) is smaller than that measured for larger indentation. Moreover, the pressure/indentation distance curves show hysteresis and the recovery takes place on a timescale that may well involve active processes and remodeling of the cell surface. These results suggest that parts of the cell membrane are not attached strongly to the underlying cytoskeleton, and these interactions increase with larger indentations. It is unlikely that this effect is due to glycocalyx on the cell surface because the surface of these cells is easily accessible to the patch pipette and we have carried out single channel recording on these cells previously (42,44,48). The presence of the submembrane space may provide an additional general mechanism for the cell to detect and respond to small mechanical forces, for example like those related to changes of osmolarity. In our previous study of the mechanisms of aldosterone action (49), we suggested that redistribution of the cell

volume caused by the observed lateral contraction results in apical swelling that, in turn, disrupts the epithelial sodium channel's interaction with the F-actin cytoskeleton. This would open the channels, increasing sodium transport. Our current observation of a submembrane space supports this hypothesis, and may represent a general mechanism for osmoregulation. In addition the presence of this ''soft'' submembrane space may explain some of the difficulties with imaging of the surface of living cells using the force-based methods of the AFM.

CONCLUSION

We have presented, to our knowledge, a new noncontact method of applying controlled force to soft living cell surfaces. It is based on the application of positive and negative pressure via a pipette and measuring the resulting surface deformation. The method can probe the mechanical properties of living cells on the nanoscale at defined positions on the cell surface. We have shown that it can exert sufficiently small forces to resolve different mechanical elements of the cell, and that the measured mechanical properties can be related to the cell topography because the cell surface can be imaged first using no pressure. This work can be straightforwardly extended to noncontact mapping of both the mechanical properties of the cell and mechanosensitive ion channels. This method therefore seems well suited to probe quantitatively the nanomechanical properties of living cells.

SUPPLEMENTARY MATERIAL

To view all of the supplemental files associated with this article, visit www.biophysj.org.

We thank Dr Catherine Williamson and Victoria Geenes for kindly providing the red blood cells and Professor Sian Harding (National Heart and Lung Institute, Imperial College) for providing cardiac cells. We also thank Dr Igor Vodyanoy and Dr Sang-Joon Cho for constructive comments during this work.

This work was funded by the Biotechnology and Biological Sciences Research Council and Glaxo SmithKline.

REFERENCES

1. Moe, P. C., P. Blount, and C. Kung. 1998. Functional and structural conservation in the mechanosensitive channel MscL implicates elements crucial for mechanosensation. *Mol. Microbiol.* 28:583–592.
2. French, A. S. 1992. Mechanotransduction. *Annu. Rev. Physiol.* 54: 135–152.
3. Morris, C. E. 1990. Mechanosensitive ion channels. *J. Membr. Biol.* 113:93–107.
4. Yang, X. C., and F. Sachs. 1989. Block of stretch-activated ion channels in *Xenopus* oocytes by gadolinium and calcium-ions. *Science.* 243:1068–1071.
5. Ali, M. H., and P. T. Schumacker. 2002. Endothelial responses to mechanical stress: where is the mechanosensor? *Crit. Care Med.* 30: S198–S206.
6. Hamill, O. P., and B. Martinac. 2001. Molecular basis of mechanotransduction in living cells. *Physiol. Rev.* 81:685–740.
7. Ingber, D. E. 1998. Cellular basis of mechanotransduction. *Biol. Bull.* 194:323–325.
8. Lehoux, S., Y. Castier, and A. Tedgui. 2006. Molecular mechanisms of the vascular responses to hemodynamic forces. *J. Intern. Med.* 259: 381–392.
9. Hamill, O. P. 2006. Twenty odd years of stretch-sensitive channels. *Pflugers Arch.* 453:333–351.
10. Hochmuth, R. M. 2000. Micropipette aspiration of living cells. *J. Biomech.* 33:15–22.
11. Dai, J. W., and M. P. Sheetz. 1995. Mechanical-properties of neuronal growth cone membranes studied by tether formation with laser optical tweezers. *Biophys. J.* 68:988–996.
12. Guck, J., R. Ananthakrishnan, H. Mahmood, T. J. Moon, C. C. Cunningham, and J. Käs. 2001. The optical stretcher: a novel laser tool to micromanipulate cells. *Biophys. J.* 81:767–784.
13. Weihs, D., and M. A. Teitel. 2006. Bio-microrheology: a frontier in microrheology. *Biophys. J.* 91:4296–4305.
14. Kuznetsova, T. G., M. N. Starodubtseva, N. I. Yegorenkov, S. A. Chizhik, and R. I. Zhdaniv. 2007. Atomic force microscopy probing of cell elasticity. *Micron.* 38:824–833.
15. Dulinska, I., M. Targosz, W. Strojny, M. Lekka, P. Czuba, W. Balwierz, and M. Szymonski. 2006. Stiffness of normal and pathological erythrocytes studied by means of atomic force microscopy. *J. Biochem. Biophys. Methods.* 66:1–11.
16. Haberle, W., J. K. H. Horber, and G. Binnig. 1991. Force microscopy on living cells. *J. Vac. Sci. Technol. B.* 9:1210–1213.
17. Lu, Y.-B., K. Franze, G. Seifert, C. Steinhäuser, F. Kirchhoff, H. Wolburg, J. Guck, P. Janmey, E.-Q. Wei, J. Käs, and A. Reichenbach. 2006. Viscoelastic properties of individual glial cells and neurons in the CNS. *Proc. Natl. Acad. Sci. USA.* 47:17759–17764.
18. Lieber, S. C., N. Aubry, J. Pain, G. Diaz, S.-J. Kim, and S. F. Vatner. 2004. Ageing increases the stiffness of cardiac myocytes measured by atomic force microscopy nanoindentation. *Am. J. Physiol. Heart Circ. Physiol.* 287:H645–H651.
19. Lekka, M., M. Fornal, G. Pyka-Fosciak, K. Lebed, B. Wizner, T. Grodzicki, and J. Styczen. 2005. Erythrocyte stiffness probed using atomic force microscope. *Biorheology.* 42:307–317.
20. Putman, C. A. J., K. O. Vanderwerf, B. G. Degrooth, N. F. Vanhulst, and J. Greve. 1994. Viscoelasticity of living cells allows high-resolution imaging by tapping mode atomic-force microscopy. *Biophys. J.* 67:1749–1753.
21. A-Hassan. E., W. F. Heinz, M. D. Antonik, N. P. D'Costa, S. Nageswaran, C.-A. Schoenenberger, and J. H. Hoh. 1998. Relative microelastic mapping of living cells by atomic force microscopy. *Biophys. J.* 74:1564–1578.
22. Pesen, D., and J. H. Hoh. 2005. Micromechanical architecture of the endothelial cell cortex. *Biophys. J.* 88:670–679.
23. Sen, S., S. Subramanian, and D. E. Discher. 2005. Indentation and adhesive probing of a cell membrane with AFM: Theoretical model and experiments. *Biophys. J.* 89:3203–3213.
24. Crick, S., and F. Yin. 2007. Assessing micromechanical properties of cells with atomic force microscopy: Importance of the contact point. *Biomech. Model. Mechanobiol.* 6:199–210.
25. Gorelik, J., A. Shevchuk, M. Ramalho, M. Elliott, C. Lei, C. F. Higgins, M. J. Lab, D. Klenerman, N. Krauzewicz, and Y. Korchev. 2002. Scanning surface confocal microscopy for simultaneous topographical and fluorescence imaging: Application to single virus-like particle entry into a cell. *Proc. Natl. Acad. Sci. USA.* 99:16018–16023.
26. Gorelik, J., Y. J. Zhang, A. I. Shevchuk, G. I. Frolenkov, D. Sanchez, M. J. Lab, I. Vodyanoy, C. R. W. Edwards, D. Klenerman, and Y. E. Korchev. 2004. The use of scanning ion conductance microscopy to image A6 cells. *Mol. Cell. Endocrinol.* 217:101–108.
27. Gorelik, J., A. I. Shevchuk, G. I. Frolenkov, I. A. Diakonov, M. J. Lab, C. J. Kros, G. P. Richardson, I. Vodyanoy, C. R. W. Edwards, D.

Klenerman, and Y. E. Korchev. 2003. Dynamic assembly of surface structures in living cells. *Proc. Natl. Acad. Sci. USA.* 100:5819–5822.

28. Zhang, Y. J., J. Gorelik, D. Sanchez, A. Shevchuk, M. Lab, I. Vodyanoy, D. Klenerman, C. Edwards, and Y. Korchev. 2005. Scanning ion conductance microscopy reveals how a functional renal epithelial monolayer maintains its integrity. *Kidney Int.* 68:1071–1077.
29. Shevchuk, A. I., G. I. Frolenkov, D. Sanchez, P. S. James, N. Freedman, M. J. Lab, R. Jones, D. Klenerman, and Y. E. Korchev. 2006. Imaging proteins in membranes of living cells by high-resolution scanning ion conductance microscopy. *Angew. Chem. Int. Ed.* 45: 2212–2216.
30. Shevchuk, A. I., J. Gorelik, S. E. Harding, M. J. Lab, D. Klenerman, and Y. E. Korchev. 2001. Simultaneous measurement of Ca^{2+} and cellular dynamics: combined scanning ion conductance and optical microscopy to study contracting cardiac myocytes. *Biophys. J.* 81: 1759–1764.
31. Korchev, Y. E., M. Milovanovic, C. L. Bashford, D. C. Bennett, E. V. Sviderskaya, I. Vodyanoy, and M. J. Lab. 1997. Specialized scanning ion-conductance microscope for imaging of living cells. *J. Microsc.* 188:17–23.
32. Korchev, Y. E., C. L. Bashford, M. Milovanovic, I. Vodyanoy, and M. J. Lab. 1997. Scanning ion conductance microscopy of living cells. *Biophys. J.* 73:653–658.
33. Cook, S. M., T. E. Schäffer, K. M. Chynoweth, M. Wigton, R. W. Simmonds, and K. M. Lang. 2006. Practical implementation of dynamic methods for measuring atomic force microscope cantilever spring constants. *Nanotechnology.* 17:2135–2145.
34. Ying, L. M., A. Bruckbauer, A. M. Rothery, Y. E. Korchev, and D. Klenerman. 2002. Programmable delivery of DNA through a nanopipet. *Anal. Chem.* 74:1380–1385.
35. Hartley, P., F. Grieser, P. Mulvaney, and G. Stevens. 1999. Surface forces and deformation at the oil-water interface probed using AFM force measurement. *Langmuir.* 15:7282–7289.
36. Attard, P., and S. J. Miklavioc. 2001. Effective spring constant of bubbles and droplets. *Langmuir.* 17:8217–8223.
37. Johnson, K. L. 1985, Contact Mechanics 56–59. Cambridge University Press, Cambridge, UK.
38. Bremmell, K. E., A. Evans, and C. A. Prestidge. 2006. Deformation and nano-rheology of red blood cells: An AFM investigation. *Colloids Surf. B Biointerfaces.* 50:43–48.
39. Anshu, B., A. B Mathur, A. M. Collinsworth, W. M. Reichert, W. E. Kraus, and G. A. Truskey. 2001. Endothelial, cardiac muscle and skeletal muscle exhibit different viscous and elastic properties as determined by atomic force microscopy. *J. Biomech.* 34:1545–1553.
40. Hoh, J. H., and C. A. Schoenenberger. 1994. Surface morphology and mechanical properties of MDCK monolayers by atomic force microscopy. *J. Cell Sci.* 107:1105–1114.
41. Steltenkamp, S., C. Rommel, J. Wegener, and A. Janshoff. 2006. Membrane stiffness of animal cells challenged by osmotic stress. *Small.* 2:1016–1020.
42. Gu, Y. C., J. Gorelik, H. A. Spohr, A. Shevchuk, M. J. Lab, S. E. Harding, I. Vodyanoy, D. Klenerman, and Y. E. Korchev. 2002. High-resolution scanning patch-clamp: new insights into cell function. *FASEB J.* 16:748–750.
43. Sanchez, D., U. Anand, J. Gorelik, C. D. Benham, C. Bountra, M. Lab, D. Klenerman, R. Birch, P. Anand, and Y. Korchev. 2007. Localized and noncontact mechanical stimulation of dorsal root ganglion sensory neurons using scanning ion conductance microscopy. *J. Neurosci. Methods.* 159:26–34.
44. Korchev, Y. E., Y. A. Negulyaev, C. R. W. Edwards, I. Vodyanoy, and M. J. Lab. 2000. Functional localization of single active ion channels can the surface of a living cell. *Nat. Cell Biol.* 2:616–619.
45. Charras, G. T., and M. A. Horton. 2002. Single cell mechanotransduction and its modulation analyzed by atomic force microscope indentation. *Biophys J.* 82:2970–2981.
46. Domke, J., and M. Radmacher. 1998. Measuring the elastic properties of thin polymer films with the atomic force microscope. *Langmuir.* 14:3320–3325.
47. Dimitriadis, E. K., F. Horkay, J. Maresca, B. Kachar, and R. S. Chadwick. 2002. Determination of elastic moduli of thin layers of soft material using the atomic force microscope. *Biophys. J.* 86:1777–1793.
48. Gorelik, J., Y. Gu, H. A. Spohr, A. I. Shevchuk, M. J. Lab, S. E. Harding, C. R. W. Edwards, M. Whitaker, G. W. J. Moss, D. C. H. Benton, D. Sánchez, A. Darszon, I. Vodyanoy, D. Klenerman, and Y. E. Korchev. 2002. Ion channels in small cells and subcellular structures can be studied with a smart patch-clamp system. *Biophys. J.* 83:3296–3303.
49. Gorelik, J., Y. J. Zhang, D. Sanchez, A. Shevchuk, G. Frolenkov, M. Lab, D. Klenerman, C. Edwards, and Y. Korchev. 2005. Aldosterone acts via an ATP autocrine/paracrine system: the Edelman ATP hypothesis revisited. *Proc. Natl. Acad. Sci. USA.* 102:15000–15005.